3D Electromagnetic Signal Processing

3D Electromagnetic Signal Processing

Davide Dardari
DEI, University of Bologna and WiLab-CNIT, Cesena Campus, Cesena (FC), Italy - (e-mail: davide.dardari@unibo.it)

***Abstract*—In this paper, we investigate the dynamic scattering array (DSA), a versatile 3D structure capable of performing joint wave-based computing and radiation by moving the processing from the digital domain to the electromagnetic (EM) domain. We provide a general analytical framework for modeling DSAs, introduce specific design algorithms, and apply them to some use cases. The examples presented in the numerical results demonstrate the potential of DSAs to further reduce complexity and the number of radiofrequency (RF) chains in holographic multiple-input multiple-output (MIMO) systems while achieving enhanced EM wave processing and radiation flexibility for tasks such as beamforming and multi-user MIMO.**

I. Introduction

Next-generation wireless systems are expected to provide enhanced performance in terms of capacity, reduced latency, and new functionalities such as integrated sensing and communication [1], [2]. This trend is driving the investigation of fundamental limits using physically consistent models, new technologies, and novel design paradigms to approach them [3], [4].

In this context, the recently introduced *holographic communications* paradigm is envisioned as a holistic way to manipulate, with unprecedented flexibility, the electromagnetic (EM) field generated or sensed by an antenna [5]. It involves designing innovative solutions capable of approaching the fundamental limits imposed by the wireless channel through the massive deployment of reconfigurable intelligent surfaces (RISs) [6], extremely large antenna arrays (ELAA) [7], and large intelligent surfaces (LISs), also known as holographic MIMO [8]–[10]. In particular, holographic MIMO surfaces are envisioned as an efficient implementation of large antenna systems, advancing beyond massive MIMO and ELAAs [10]. In holographic MIMO, the density of the antenna elements is increased, ideally approaching a continuous distribution, which allows for highly flexible manipulation of EM waves. Closely spaced antenna elements (below $\lambda/2$, with λ being the wavelength) do not significantly increase the exploitable degrees-of-freedom (DoF) of the channel [9], [11]. Nevertheless, when the spacing of the elements is made very small, strong coupling occurs, and the gain of a linear array shifts from N, as in conventional arrays, to N^2, being N the number of antenna elements, resulting in the so-called "superdirectivity" [12]. While achieving very narrow beams is highly desirable in many contexts, the superdirectivity effect is only obtained in the end-fire direction of the array and can lead to extremely high driving currents corresponding to high Q-factor values (and hence a lower bandwidth) [13]. Exploiting higher frequency bands, such as millimeter wave and THz, opens up the potential to utilize the extra DoF provided by the channel in the radiating near-field propagation region, even under line-of-sight (LOS) conditions [14]–[18].

The utilization of high-frequency bands in the millimeter wave and THz ranges, coupled with the integration of antennas with a very large number of elements, is pushing current technology towards insurmountable barriers in hardware complexity and power consumption. This issue, also known as *digital bottleneck*, poses serious challenges for the sustainability of future wireless networks. In MIMO-based systems, hybrid digital-analog solutions have been extensively explored to partially alleviate these issues by reducing the number of radiofrequency (RF) chains and the digital processing burden, albeit at the expense of flexibility [19].

A promising approach toward sustainability is to delegate part of the signal processing directly to the EM level, known as electromagnetic signal and information theory (ESIT) [20]–[22]. This can be achieved by designing reconfigurable EM environments [23] using novel EM metamaterials devices to perform basic processing functions (e.g., spatial first derivative) [24], RISs, or the recently introduced stacked intelligent metasurfaces (SIMs) [25]. The study of SIM is still in its infancy, and the main technological and modeling challenges have yet to be fully identified. For instance, the distance between the layers must be several wavelengths to validate the currently adopted cascade model. Power losses and signal distortion caused by the multiple layers and the bounding box require further investigation. A key limitation of SIMs is that only the final layer radiates, constraining the EM wave characteristics to those achievable with a classical planar surface or array, while the role of the hidden layers is to perform an EM transformation.

To overcome the aforementioned issues, we investigate a 3D EM antenna structure, termed DSA, that offers significant flexibility by providing enhanced processing capabilities directly at the EM level. Specifically, a DSA consists of a limited number of active antenna elements, each associated with an RF chain, surrounded by a cloud of reconfigurable passive scatterers that interact with each other in the reactive near field so that EM processing and radiation are performed jointly "over the air". A DSA can be considered as a generalization of reactively controlled arrays, originally proposed in [26], and their evolution toward electrically steerable passive array radiators (ESPARs) in which a single RF chain is considered [27]. In particular, we first characterize the input-output characteristic of the DSA as a function of its configuration parameters. Subsequently, we propose a strategy to optimize these parameters according to the desired processing functionality and apply this strategy to two different use cases of interest:

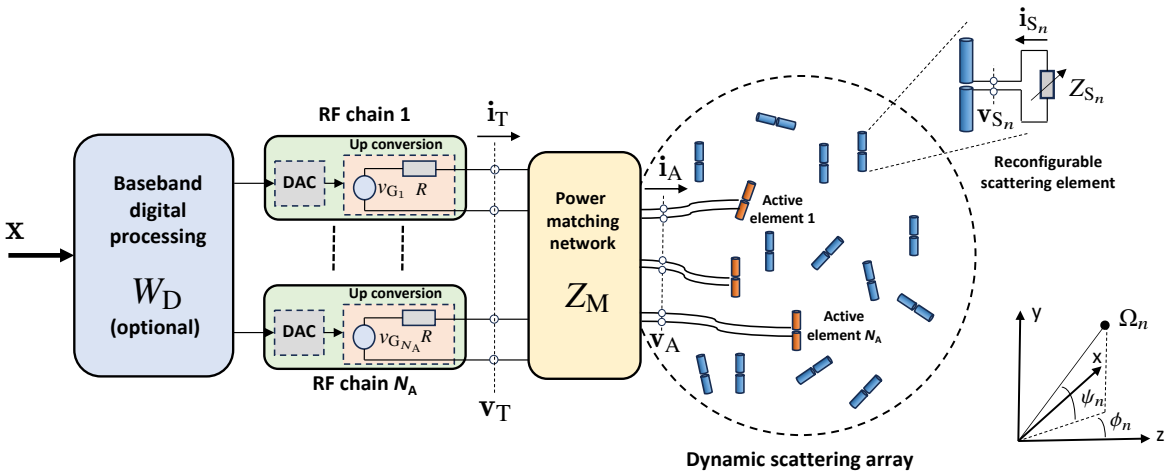

Fig. 1. Principle scheme of a dynamic scattering array.

beamforming and MIMO. Numerical results for each use case demonstrate the great flexibility of the DSA in performing various signal processing tasks by offering several advantages in terms of size reduction while minimizing the number of RF chains. For instance, we will show that the tight coupling of DSA elements allows for the realization of superdirectivity behavior independently of the beam's direction, in contrast to standard arrays where superdirectivity can only be achieved in the end-fire direction [13], [28].

The results obtained in this paper demonstrate the potential of DSA to realize wave-based computation "over the air" by leveraging the coupling between active and scattering elements, thus minimizing the number of RF chains and baseband processing in the digital domain. This is achieved through a semi-passive structure with minimal energy consumption and nearly zero latency, as the processing occurs at the speed of light.

II. Dynamic Scattering Array (DSA) Modeling

We consider the transmitting system illustrated in Fig. 1, where the DSA is composed of N_A active antenna elements surrounded by a cloud of N_S reconfigurable passive scatterers. The nth element (active or passive) of the DSA, with $n = 1, 2, \ldots N$, $N = N_A + N_S$, is located in position $\mathbf{p}_n$. The nth scatterer, with $n = 1, 2, \ldots N_S$, is itself an antenna element terminated by a reconfigurable impedance load $Z_{S_n}(\theta_n)$. To avoid power dispersion, we impose that the load is purely reactive, i.e., $Z_{S_n}(\theta_n) = \jmath\theta_n$, where $\theta_n \in \mathbb{R}$ is the reconfigurable reactance. Denote with $\boldsymbol{\theta} = \left[\theta_1, \theta_2, \ldots, \theta_{N_S}\right]^{\mathsf{T}}$ the set of reconfigurable reactances and with $\mathbf{Z}_S(\boldsymbol{\theta}) = \text{diag}\left(Z_{S_1}(\theta_1), Z_{S_2}(\theta_2), \ldots, Z_{S_{N_S}}(\theta_{N_S})\right)$ the corresponding set of loads.

The DSA can be modeled as a linear N-port network. Specifically, in a compact description, we define $\mathbf{v}_A \in \mathbb{C}^{N_A \times 1}$ and $\mathbf{i}_A \in \mathbb{C}^{N_A \times 1}$ the complex voltage and current envelopes (in the following denoted simply as voltages and currents) at the ports of the N_A active antennas (i.e., the input ports of the DSA), and $\mathbf{v}_S \in \mathbb{C}^{N_S \times 1}$ and $\mathbf{i}_S \in \mathbb{C}^{N_S \times 1}$ the voltages and currents at the ports of the N_S scatterers. We collect all the currents and voltages at the N ports of the DSA in the vectors

$$\mathbf{i} = \begin{bmatrix} \mathbf{i}_A \\ \mathbf{i}_S \end{bmatrix} \qquad \mathbf{v} = \begin{bmatrix} \mathbf{v}_A \\ \mathbf{v}_S \end{bmatrix}. \tag{1}$$

All the interactions between the elements of the DSA are captured by the impedance matrix $\mathbf{Z} \in \mathbb{C}^{2N \times 2N}$, which does not depend on the reconfigurable loads, and relates the voltages and currents of the N ports as $\mathbf{v} = \mathbf{Z}\,\mathbf{i}$. In particular, the (n, m)th element of $\mathbf{Z}$ represents the mutual coupling coefficient between the nth and mth elements obtained as the ratio between the open-circuit voltage observed at the mth port and the excitation current applied to the nth port supposing that the remaining ports are kept open (no current flow) [29]. It is convenient to divide the impedance matrix $\mathbf{Z}$ into the sub-matrices $\mathbf{Z}_{AA}$, $\mathbf{Z}_{AS}$, $\mathbf{Z}_{SA}$, and $\mathbf{Z}_{SS}$ so that we can write

$$\begin{bmatrix} \mathbf{v}_A \\ \mathbf{v}_S \end{bmatrix} = \begin{bmatrix} \mathbf{Z}_{AA} & \mathbf{Z}_{AS} \\ \mathbf{Z}_{SA} & \mathbf{Z}_{SS} \end{bmatrix} \cdot \begin{bmatrix} \mathbf{i}_A \\ \mathbf{i}_S \end{bmatrix}. \tag{2}$$

The voltages $\mathbf{v}_A$ and currents $\mathbf{i}_A$ at the input ports of the DSA are related by the input impedance of the DSA $\mathbf{Z}_A(\boldsymbol{\theta}) \in \mathbb{C}^{N_A \times N_A}$ as $\mathbf{v}_A = \mathbf{Z}_A(\boldsymbol{\theta})\,\mathbf{i}_A$. By elaborating (2) and considering that at the scatterers' ports it is $\mathbf{v}_S = -\mathbf{Z}_S(\boldsymbol{\theta})\,\mathbf{i}_S$, we obtain

$$\mathbf{Z}_A(\boldsymbol{\theta}) = \mathbf{Z}_{AA} - \mathbf{Z}_{AS}\left(\mathbf{Z}_{SS} + \mathbf{Z}_S(\boldsymbol{\theta})\right)^{-1}\mathbf{Z}_{SA} \tag{3}$$

which depends on parameters $\boldsymbol{\theta}$ through the scatterers' loads $\mathbf{Z}_S(\boldsymbol{\theta})$.

The N_A active elements are connected to N_A RF chains, including digital-to-analog converters (DACs) and up-conversion stages, through a $2N_A$-port power matching network whose purpose is to maximize the power transfer between the RF chains and the DSA. The relationship between the voltages and the currents present at the ports of the matching network is given by

$$\begin{bmatrix} \mathbf{v}_T \\ \mathbf{v}_A \end{bmatrix} = \mathbf{Z}_M(\boldsymbol{\theta}) \begin{bmatrix} \mathbf{i}_T \\ -\mathbf{i}_A \end{bmatrix} \tag{4}$$

where, assuming no losses in the power matching network, $\mathbf{Z}_{\mathrm{M}}(\boldsymbol{\theta})$ is equal to [28]

$$\mathbf{Z}_{\mathrm{M}}(\boldsymbol{\theta}) = \begin{bmatrix} \mathbf{0}_{N_{\mathrm{A}}} & -\jmath\sqrt{R}\,\Re\left\{\mathbf{Z}_{\mathrm{A}}(\boldsymbol{\theta})\right\}^{\frac{1}{2}} \\ -\jmath\sqrt{R}\,\Re\left\{\mathbf{Z}_{\mathrm{A}}(\boldsymbol{\theta})\right\}^{\frac{1}{2}} & -\jmath\Im\left\{\mathbf{Z}_{\mathrm{A}}(\boldsymbol{\theta})\right\} \end{bmatrix} \tag{5}$$

with R being the output resistance of each RF chain, $\Re\{x\}$ and $\Im\{x\}$ denoting, respectively, the real and imaginary parts of x. As it can be noticed from (5), the matching network depends on the DSA input impedance $\mathbf{Z}_{\mathrm{A}}(\boldsymbol{\theta})$ and hence on the parameters $\boldsymbol{\theta}$. Therefore, the matching network should be reconfigured for a given DSA configuration to maximize the power transfer. It turns out that $\mathbf{v}_{\mathrm{T}} = \mathbf{Z}_{\mathrm{T}}\,\mathbf{i}_{\mathrm{T}}$, with $\mathbf{Z}_{\mathrm{T}} = R\,\mathbf{I}_{N_{\mathrm{A}}}$ and, assuming lossless antenna elements, the transmitted power corresponds to the radiated power P_{rad} given by $P_{\mathrm{T}} = P_{\mathrm{rad}} = \mathbb{E}\left\{\mathbf{i}_{\mathrm{A}}^{\mathsf{H}}\,\Re\left\{\mathbf{Z}_{\mathrm{A}}(\boldsymbol{\theta})\right\}\,\mathbf{i}_{\mathrm{A}}\right\} = \mathbb{E}\left\{\mathbf{v}_{\mathrm{T}}^{\mathsf{H}}\,\mathbf{v}_{\mathrm{T}}\right\}/R$, where $\mathbb{E}\{\cdot\}$ denotes the statistical expectation.

We also foresee an optional baseband linear processing block implemented in the digital domain (digital precoder), described by the matrix $\mathbf{W}_{\mathrm{D}} \in \mathbb{C}^{N_{\mathrm{A}}\times N_{\mathrm{A}}}$, whose input is represented by the information vector $\mathbf{x} \in C^{N_{\mathrm{A}}\times 1}$ to be transmitted. The matrix $\mathbf{W}_{\mathrm{D}}$ relates the transmitted information vector $\mathbf{x}$ and the voltages $\mathbf{v}_{\mathrm{T}}$ at the input of the matching network, i.e., $\mathbf{v}_{\mathrm{T}} = \mathbf{W}_{\mathrm{D}}\,\mathbf{x}$. In the following, we impose the arbitrarily normalization $\|\mathbf{W}_{\mathrm{D}}\|_{\mathrm{F}} = \sqrt{R\,N_{\mathrm{A}}}$, with $\|\cdot\|_{\mathrm{F}}$ denoting the Frobenius Norm. Such a normalization ensures that $\mathbb{E}\left\{\mathbf{x}^{\mathsf{H}}\,\mathbf{x}\right\} = P_{\mathrm{T}}$, as typically considered in the signal processing community. The reconfigurable reactances $\boldsymbol{\theta}$ along with the elements of matrix $\mathbf{W}_{\mathrm{D}}$ represent the set of parameters to be optimized to obtain the desired processing functionality, as will be described later.

By combining (4) and (5), we obtain a compact relationship between the information vector $\mathbf{x}$ and the total current $\mathbf{i}$ flowing in the DSA

$$\mathbf{i} = \mathbf{W}_{\mathrm{EM}}(\boldsymbol{\theta})\,\mathbf{W}_{\mathrm{D}}\,\mathbf{x} \tag{6}$$

where

$$\mathbf{W}_{\mathrm{EM}}(\boldsymbol{\theta}) = \frac{1}{\jmath\sqrt{R}} \begin{bmatrix} \Re\left\{\mathbf{Z}_{\mathrm{A}}(\boldsymbol{\theta})\right\}^{-\frac{1}{2}} \\ -\left(\mathbf{Z}_{\mathrm{SS}} + \mathbf{Z}_{\mathrm{S}}(\boldsymbol{\theta})\right)^{-1}\mathbf{Z}_{\mathrm{SA}}\,\Re\left\{\mathbf{Z}_{\mathrm{A}}(\boldsymbol{\theta})\right\}^{-\frac{1}{2}} \end{bmatrix} \tag{7}$$

accounts for the EM-level signal processing operated by the reconfigurable DSA as a function of the parameters $\boldsymbol{\theta}$.

Consider now K test points located in positions $\mathbf{t}_k$, with $k = 1, 2, \ldots, K$, and that in each test point, a conventional receiving antenna is used to receive the signal with gain G_{R}. As commonly done in the literature, we assume that $|\mathbf{t}_k - \mathbf{p}_n| \gg \lambda$, $\forall k, n$, that is, the test points are located in the radiative region of the antenna structure and the receiving antennas do not affect the transmitting DSA. As an example, the set of K antennas could represent a conventional receiving antenna array of a MIMO system. The useful component (i.e., without noise) of the received signal at the test positions is

$$\mathbf{y} = \mathbf{H}_{\mathrm{c}}\,\mathbf{i} = \mathbf{H}_{\mathrm{c}}\,\mathbf{W}_{\mathrm{EM}}(\boldsymbol{\theta})\,\mathbf{W}_{\mathrm{D}}\,\mathbf{x} = \mathbf{H}(\boldsymbol{\theta}, \mathbf{W}_{\mathrm{D}})\,\mathbf{x} \tag{8}$$

where $\mathbf{H}_{\mathrm{c}}$ is the transimpedance matrix of the radio channel accounting for the propagation effects and $\mathbf{H}(\boldsymbol{\theta}, \mathbf{W}_{\mathrm{D}})$ is the end-to-end baseband equivalent channel matrix as commonly defined in signal processing.

III. DSA Optimization

In this section, we illustrate a possible optimization strategy of the DSA along with its application to 2 different use cases. Numerical results associated with each use case will be reported in Sec. IV.

A. Joint Optimization of the DSA and the Digital Precoder

For a given propagation scenario characterized by the transimpedance matrix $\mathbf{H}_{\mathrm{c}}$ and K test points, suppose we fix a specification $\mathbf{H}_{\mathrm{opt}}$ on the desired end-to-end channel matrix. The reconfigurable parameters of the DSA and the digital precoder can be designed by solving the following constrained optimization problem:

$$\begin{aligned} &\underset{\boldsymbol{\theta},\,\mathbf{W}_{\mathrm{D}},\,\alpha}{\text{minimize}} \left\|\alpha\,\mathbf{H}_{\mathrm{c}}\,\mathbf{W}_{\mathrm{EM}}(\boldsymbol{\theta})\,\mathbf{W}_{\mathrm{D}} - \mathbf{H}_{\mathrm{opt}}\right\|_{\mathrm{F}} \\ &s.t. \quad \|\mathbf{W}_{\mathrm{D}}\|_{\mathrm{F}}^2 = R\,N_{\mathrm{A}} \end{aligned} \tag{9}$$

where the scalar $\alpha \in \mathbb{R}$ accounts for the possible lack in the link budget to achieve $\mathbf{H}_{\mathrm{opt}}$ that has to be eventually coped with increased transmitted power.

Unfortunately, in general, the constrained optimization problem in (9) is not convex thus making its numerical solution more challenging. A possible approach to translating it into an unconstrained optimization problem is to resort to the following alternate optimization procedure:

- STEP 0: We set the candidate vector $\hat{\boldsymbol{\theta}}$ to an initial guess value, for instance randomly chosen or equal to zero.
- STEP 1: For a fixed $\hat{\boldsymbol{\theta}}$, it is possible to find in closed form the values of $\mathbf{W}_{\mathrm{D}}$ and α that minimize the objective function and satisfy the constraint in (9). In particular, we solve the following equation

  $$\alpha\,\mathbf{H}_{\mathrm{c}}\,\mathbf{W}_{\mathrm{EM}}(\hat{\boldsymbol{\theta}})\,\mathbf{W}_{\mathrm{D}} = \mathbf{H}_{\mathrm{opt}} \tag{10}$$

  of which the minimum norm solution is

  $$\alpha\mathbf{W}_{\mathrm{D}} = \left(\mathbf{H}_{\mathrm{c}}\,\mathbf{W}_{\mathrm{EM}}(\hat{\boldsymbol{\theta}})\right)^{\dagger}\mathbf{H}_{\mathrm{opt}} \tag{11}$$

  with $\mathbf{A}^{\dagger}$ denoting the pseudo-inverse of matrix $\mathbf{A}$.
  The corresponding values of $\hat{\alpha}$ and $\hat{\mathbf{W}}_{\mathrm{D}}$ are, therefore,

  $$\hat{\alpha} = \frac{1}{\sqrt{R\,N_{\mathrm{A}}}}\left\|\left(\mathbf{H}_{\mathrm{c}}\,\mathbf{W}_{\mathrm{EM}}(\hat{\boldsymbol{\theta}})\right)^{\dagger}\mathbf{H}_{\mathrm{opt}}\right\|_{\mathrm{F}} \tag{12}$$

  and

  $$\hat{\mathbf{W}}_{\mathrm{D}} = \frac{1}{\hat{\alpha}}\left(\mathbf{H}_{\mathrm{c}}\,\mathbf{W}_{\mathrm{EM}}(\hat{\boldsymbol{\theta}})\right)^{\dagger}\mathbf{H}_{\mathrm{opt}}\,. \tag{13}$$

- STEP 2: Starting from the candidates $\hat{\alpha}$ and $\hat{\mathbf{W}}_{\mathrm{D}}$ from STEP 1, the following unconstrained minimization problem involving only $\boldsymbol{\theta}$ is solved numerically

  $$\hat{\boldsymbol{\theta}} = \arg\min_{\boldsymbol{\theta}} \left\|\hat{\alpha}\,\mathbf{H}_{\mathrm{c}}\,\mathbf{W}_{\mathrm{EM}}(\hat{\boldsymbol{\theta}})\,\mathbf{W}_{\mathrm{D}} - \mathbf{H}_{\mathrm{opt}}\right\|_{\mathrm{F}}\,. \tag{14}$$

- STEP 3: Repeat STEPS 1 and 2 for a given number N_{alt} iterations or until no significant variations of the parameters take place.

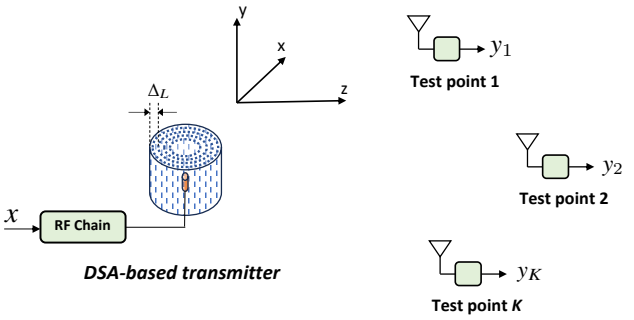

Fig. 2. Use case 1: Single RF chain DSA for high gain beamforming.

The inclusion of the digital precoder, while not strictly necessary, may aid in the optimization process of the DSA by handling a portion of the processing when $N_\mathrm{A} > 1$. If omitted, we set $\hat{\mathbf{W}}_\mathrm{D} = \mathbf{W}_\mathrm{D} = \sqrt{R}\,\mathbf{I}$, and only proceed with STEP 2 once.

B. Use Case 1: Beam Forming

Suppose we want to design a single-input DSA ($N_\mathrm{A} = 1$, no digital precoding) realizing a generic radiation diagram, for instance, imposing that at the test locations $\mathbf{t}_k$, the channel matrix $[\mathbf{H}_\mathrm{opt}]_{k,1}$, $k = 1, 2, \ldots, K$, assumes the desired value (see Fig. 2). For instance, one might define a uniform set of test points $\mathbf{t}_k = [d \sin\phi_k, 0, d\cos\phi_k]^\mathsf{T}$ on the $x-z$ plane a distance d in the far-field region of the DSA, with $\phi_k = 2\pi k/K$, and maximize the radiation diagram at the $k = \tilde{k}$th direction $\phi_{\tilde{k}}$ (beam steering). This can be achieved by setting $[\mathbf{H}_\mathrm{opt}]_{k,1} = \sqrt{P_\mathrm{R}}$, for $k = \tilde{k}$, and zero otherwise, being P_R the desired received power. Incidentally, after the optimization process, the resulting parameter $\hat{\alpha}^2$ will represent the required transmitted power P_T to satisfy the link budget. It is worth noticing that, in principle, only the optimization at the single test point $\mathbf{t}_{\tilde{k}}$, i.e., $K = 1$, would suffice to obtain the desired beam steering result. However, the addition of many other test points set to zero helps the minimization algorithm to speed up and avoid the convergence to bad local minima.

C. Use Case 2: Multi-layer MIMO Communication

In this use case, we consider a MIMO communication with a receiving conventional uniform linear array (ULA) with K elements spaced at $\lambda/2$. The purpose is to design the DSA in such a way an optimal multi-layer MIMO link is established between the transmitter and the receiver. It is well known from MIMO theory that for a given generic propagation scenario with channel transimpedance matrix $\mathbf{H}_\mathrm{c}$ characterized by rank r, up to r parallel orthogonal links (layers) can be established between the transmitter and the receiver on which independent data stream can be transmitted [30]. To exploit all of them, it must be $N_\mathrm{A} = r$ and the DSA must implement a suitable precoding strategy, i.e., act as an *EM precoder*.

Let us introduce the singular value decomposition (SVD) of the channel transimpedance $\mathbf{H}_\mathrm{c} = \mathbf{U}\,\mathbf{\Lambda}\,\mathbf{V}^\mathsf{H}$, where $\mathbf{U}$ and $\mathbf{V}$ contain the left and right eigenvectors, respectively, and

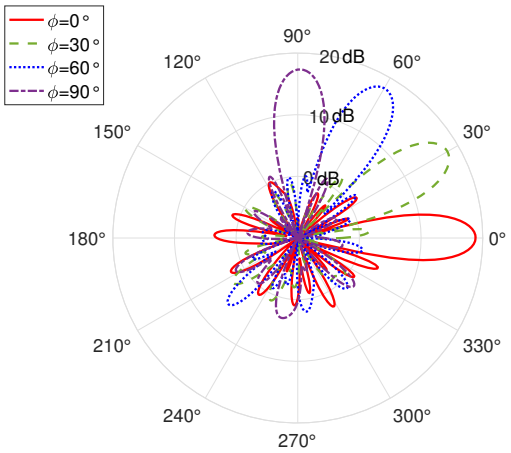

Fig. 3. Radiation diagram of a disk-shaped DSA ($L_\mathrm{R} = 1$), with Δ_L and $L = 5$, exhibiting a super directive characteristic.

$\mathbf{\Lambda}$ is a diagonal matrix gathering the singular values of the channel transimpedance matrix $\mathbf{H}_\mathrm{c}$. A typical MIMO setup, assuming the channel state information (CSI) is available at the transmitter, requires a precoding operation $\mathbf{V}$ at the transmitter and a combining operation $\mathbf{U}^\mathsf{H}$ at the receiver such that the channel is diagonalized, i.e., the end-to-end channel matrix is proportional to the diagonal matrix $\mathbf{\Lambda}$. Assuming the receiver performs the combining operation $\tilde{\mathbf{y}} = \mathbf{U}^\mathsf{H}\mathbf{y}$, the MIMO channel is diagonalized if we design the DSA implementing the precoding $\mathbf{V}$ by setting $\mathbf{W}_\mathrm{EM}(\hat{\boldsymbol{\theta}})\,\mathbf{W}_\mathrm{D} = \mathbf{V}$ or, equivalently, $\mathbf{H}_\mathrm{opt} = \mathbf{U}^\mathsf{H}\,\mathbf{\Lambda}$. In this manner, it results $\tilde{\mathbf{y}} = \mathbf{U}^\mathsf{H}\mathbf{H}(\boldsymbol{\theta}, \mathbf{W}_\mathrm{D})\,\mathbf{x} = \mathbf{U}^\mathsf{H}\mathbf{H}_\mathrm{c}\,\mathbf{W}_\mathrm{EM}(\hat{\boldsymbol{\theta}})\,\mathbf{W}_\mathrm{D}\,\mathbf{x} = \mathbf{\Lambda}\,\mathbf{x}$ and N_A parallel communication layers can be established. The designed DSA implements the optimal precoding by using no more than $N_\mathrm{A} = r$ RF chains (i.e., the minimum possible value) which is much simpler and less energy consuming than any conventional full digital or hybrid solution.

IV. Numerical Results

In this section, we present some numerical results related to the use cases described in Sec. III with the purpose of validating and investigating the potential of the proposed DSA with respect to classical array structures. The following parameters have been considered in the numerical evaluations if not otherwise specified: $f_0 = 28\,\mathrm{GHz}$, $G_\mathrm{R} = 0\,\mathrm{dB}$, $R = 50\,\mathrm{Ohm}$, vertical polarization. Hertzian dipoles have been considered for an analytical evaluation of the impedance matrix $\mathbf{Z}$ [29]. The standard numerical tool based on the quasi-Newton method [31] with N_i iterations is utilized to minimize (14).

A. Beam Forming and Superdirectivity

We first investigate the beam forming capabilities of the DSA using one RF chain ($N_\mathrm{A} = 1$ active antenna element) and the deployment of the scatterers according to L concentric cylinders with incremental radius of step Δ_L and scatterers separated of $\lambda/2$ within each cylinder along the circle and the y axis (see Fig. 2). We denote with L_R the number of vertical rings composing each cylinder. The cylindric structure appears

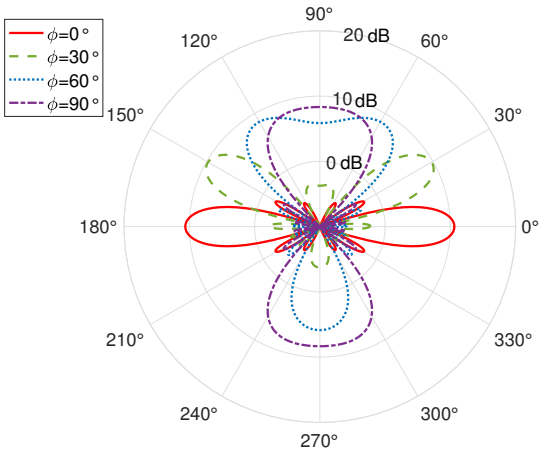

Fig. 4. Radiation pattern of a conventional ULA with $N_{\mathrm{A}} = 6$ active elements.

very appealing especially for its use in base stations or access points thanks to its circular symmetry. When $L_{\mathrm{R}} = 1$, the cylinder degenerates into a disk. Obviously, other structures can be considered as well depending on the specific application.

The target end-to-end channel matrix $\mathbf{H}_{\mathrm{opt}}$ with $K = 108$ test points deployed on the $x - z$ plane at distance $d = 100\,\mathrm{m}$ (far field) according to the use case in Sec. III-B was considered for 4 different steering angles, 0°, 30°, 60°, and 90°, respectively. Only the optimization Step 2 was performed with $N_{\mathrm{i}} = 1500$ iterations and setting $\mathbf{W}_{\mathrm{D}} = \sqrt{R}$ (in this case $\mathbf{W}_{\mathrm{D}}$ is a scalar and no digital processing takes place).

In Fig. 3, the radiation diagrams for the 4 steering angles obtained with $\Delta_L = \lambda/4$, $L = 5$, $L_{\mathrm{R}} = 1$ (disk shape), corresponding to $N_{\mathrm{S}} = 121$ scatterers are shown. As it can be observed, the gain of the DSA is independent of the angle and it is about 18.6 dB. In addition, limited back radiation is obtained without the need to insert a ground plane that would impede the steering in the angle range [90° – 270°]. As pointed out in the Introduction, the performance of any SIM is constrained by the final layer surface of the structure, therefore it is upper bounded by that one can obtain by replacing the SIM with a full digital planar or linear array with the same layout and number of elements. Therefore, for the sake of comparison, we consider the radiation diagrams obtained using a standard full-digital ULA with the same aperture of the DSA (3.2 cm diameter) in the $x - z$ plane. The corresponding radiation diagrams are reported in Fig. 4. This array requires $N_{\mathrm{A}} = 6$ active antennas compared to only one active antenna of the DSA. As well-known, in ULAs the gain degrades when approaching 90° from a maximum value of 10.6 dB (about $10\log_{10}(N_{\mathrm{A}}\,G_{\mathrm{d}})$, with $G_{\mathrm{d}} = 3/2$ the gain of the Hertzian dipole) and symmetric back radiation is present. The proposed DSA exhibits superdirectivity capability with an additional gain of 8 dB. Contrary to standard arrays, where superdirectivity is obtained only in the end-fire direction [12], here notably superdirectivity is equally obtained in all steering directions.

In Table I, the impact of the cylinders spacing Δ_L and the number of rings L_{R} is investigated. As it can be noticed, the maximum gain is obtained for $\Delta_L = \lambda/4$ confirming that superdirectivity can be achieved only by exploiting the mutual coupling between the antenna elements but, at the same time, that there is an optimum spacing value to be found. In fact, on one hand, higher spacing reduces the coupling and hence the contribution to radiation of those scatterers located far away from the active element. On the other hand, very close spacing tightens the coupling between the elements and reduces the DoF available for optimization. A higher number of rings ($L_{\mathrm{R}} = 3$) further increases the directivity by thinning the radiation diagram in the y direction. The corresponding Q-factor is in general relatively small denoting a wideband characteristic of the DSA under the considered setting and there is no need to generate very high currents as happens in conventional superdirective end-fire arrays [28]. The analysis and optimization of scatterers' deployment strategies is a topic that deserves future investigations.

TABLE I
CYLINDRIC SHAPE. $L = 5$.

Configuration	Gain (dB)	N_{S}	Q-factor
$\Delta_L = \lambda/8$, $L_{\mathrm{R}} = 1$	15	89	1.1
$\Delta_L = \lambda/6$, $L_{\mathrm{R}} = 1$	16.7	100	1.25
$\Delta_L = \lambda/4$, $L_{\mathrm{R}} = 1$	18.6	121	0.91
$\Delta_L = \lambda/2$, $L_{\mathrm{R}} = 1$	16	184	0.24
$\Delta_L = \lambda$, $L_{\mathrm{R}} = 1$	15.7	310	0.24
$\Delta_L = \lambda/4$, $L_{\mathrm{R}} = 3$	20.4	363	0.3

B. Multi-layer MIMO

Finally, we consider the scenario of use case 2 in Sec. III-C where a multi-layer MIMO link with a user located at $d = 10\,\mathrm{m}$ equipped with a standard ULA with $K = 20$ elements spaced of $\lambda/2$ has to be established in non-line-of-sight (NLOS) condition. The DSA is equipped with $N_{\mathrm{A}} = 4$ active antennas and N_{A} RF chains to allow the transmission of up to 4 data streams (layers) according to channel characteristics. The simulated NLOS channel consists of 5 multi-paths caused by the reflection of 5 scatterers located at angles $\phi = \{-43°, -14°, 14°, 43°, 72°\}$ and distance 5 m. The corresponding strongest singular values of the channel are $\mathbf{\Lambda} = \mathrm{diag}\,(-35.6\,\mathrm{dB}, -42.4\,\mathrm{dB}, -43.7\,\mathrm{dB}, -46.3\,\mathrm{dB}, -82\,\mathrm{dB}, \ldots)$, which has clearly rank $r = 4$. The DSA has the following parameters $\Delta_L = \lambda/4$, $L_{\mathrm{R}} = 1$, $N_{\mathrm{S}} = 121$, and it is optimized with $N_{\mathrm{i}} = 50$ and $N_{\mathrm{alt}} = 10$.

In Table II, the resulting coefficients $\hat{\mathbf{\Lambda}}$ of the end-to-end channel are reported. The comparison between the diagonal and off-diagonal values indicates that the coupling between different layers is completely negligible, i.e., the channel is almost perfectly diagonalized. Compared to the singular values of the channel in $\mathbf{\Lambda}$, the diagonal elements of $\hat{\mathbf{\Lambda}}$ exhibit the same behavior with a loss of about 6 dB that can be ascribed to the fact that the antenna is not ideal.

TABLE II
$\left[\hat{\Lambda}\right]_{n,k}$ IN DB, FOR $n, k = 1, 2, 3, 4$.

-41.6	-177	-190	-175
-170	-48	-185	-170
-183	-184	-49.7	-182
-164	-166	-180	-52.3

V. Conclusion

In this paper, we have investigated the dynamic scattering array (DSA) as an appealing technology aimed at shifting part of the signal processing from the digital domain to the EM domain. This is achieved through the joint optimization of EM processing and radiation of active and reconfigurable scattering elements interacting in the reactive near field. We have shown that the DSA provides unprecedented flexibility in managing the EM field by reducing or circumventing digital processing at the baseband, thereby surpassing the flexibility offered by classical MIMO and recent SIM implementations. Consequently, the reduction in RF chains and digital processing facilitates the realization of energy-efficient, low-latency, and cost-effective holographic MIMO systems, then addressing the sustainability concerns of future wireless networks.

Acknowledgment

This work was supported by the European Union under the Italian National Recovery and Resilience Plan (NRRP) of NextGeneration EU, partnership on "Telecommunications of the Future" (PE00000001 - program "RESTART"), and by the HORIZON-JU-SNS-2022-STREAM-B-01-03 6G-SHINE project (Grant Agreement No. 101095738).

References

[1] A. Dang, S., B. O., Shihada, and et al., "What should 6G be?" *Nature Electronics 3*, vol. 20-29, 2020.

[2] N. Gonzlez-Prelcic, M. Furkan Keskin, O. Kaltiokallio, M. Valkama, D. Dardari, X. Shen, Y. Shen, M. Bayraktar, and H. Wymeersch, "The integrated sensing and communication revolution for 6G: Vision, techniques, and applications," *Proceedings of the IEEE*, vol. 112, no. 7, pp. 676–723, July 2024.

[3] E. Björnson, Y. C. Eldar, E. G. Larsson, A. Lozano, and H. V. Poor, "Twenty-five years of signal processing advances for multiantenna communications: From theory to mainstream technology," *IEEE Signal Processing Magazine*, vol. 40, no. 4, pp. 107–117, 2023.

[4] C. You, Y. Cai, Y. Liu, M. Di Renzo, T. M. Duman, A. Yener, and A. L. Swindlehurst, "Next Generation Advanced Transceiver Technologies for 6G," *arXiv e-prints*, p. arXiv:2403.16458, Mar. 2024.

[5] D. Dardari and N. Decarli, "Holographic communication using intelligent surfaces," *IEEE Communications Magazine*, vol. 59, no. 6, pp. 35–41, June 2021.

[6] M. Di Renzo, F. H. Danufane, and S. Tretyakov, "Communication models for reconfigurable intelligent surfaces: From surface electromagnetics to wireless networks optimization," *Proceedings of the IEEE*, vol. 110, no. 9, pp. 1164–1209, 2022.

[7] Z. Wang, J. Zhang, H. Du, W. E. I. Sha, B. Ai, D. Niyato, and M. Debbah, "Extremely large-scale MIMO: Fundamentals, challenges, solutions, and future directions," *IEEE Wireless Communications*, pp. 1–9, 2023.

[8] D. Dardari, "Communicating with large intelligent surfaces: Fundamental limits and models," *IEEE Journal on Selected Areas in Communications*, vol. 38, no. 11, pp. 2526–2537, Nov 2020.

[9] A. A. D'Amico and L. Sanguinetti, "Holographic MIMO Communications: What is the benefit of closely spaced antennas?" *arXiv e-prints*, p. arXiv:2307.13467, Jul. 2023.

[10] T. Gong, P. Gavriilidis, R. Ji, C. Huang, G. C. Alexandropoulos, L. Wei, Z. Zhang, M. Debbah, H. V. Poor, and C. Yuen, "Holographic MIMO communications: Theoretical foundations, enabling technologies, and future directions," *IEEE Communications Surveys & Tutorials*, vol. 26, no. 1, pp. 196–257, 2024.

[11] A. S. Y. Poon and D. N. C. Tse, "Does superdirectivity increase the degrees of freedom in wireless channels?" in *2015 IEEE International Symposium on Information Theory (ISIT)*, 2015, pp. 1232–1236.

[12] M. T. Ivrlac and J. A. Nossek, "The multiport communication theory," *IEEE Circuits and Systems Magazine*, vol. 14, no. 3, pp. 27–44, 2014.

[13] L. Han, H. Yin, and T. L. Marzetta, "Coupling matrix-based beamforming for superdirective antenna arrays," in *ICC 2022 - IEEE International Conference on Communications*, 2022, pp. 5159–5164.

[14] S. Phang, M. T. Ivrla, G. Gradoni, S. C. Creagh, G. Tanner, and J. A. Nossek, "Near-field MIMO communication links," *IEEE Transactions on Circuits and Systems I: Regular Papers*, vol. 65, no. 9, pp. 3027–3036, 2018.

[15] N. Decarli and D. Dardari, "Communication modes with large intelligent surfaces in the near field," *IEEE Access*, vol. 9, pp. 165 648–165 666, 2021.

[16] Y. Liu, J. Xu, Z. Wang, X. Mu, and L. Hanzo, "Near-Field Communications: What Will Be Different?" *arXiv e-prints*, p. arXiv:2303.04003, Mar. 2023.

[17] H. Zhang, N. Shlezinger, F. Guidi, D. Dardari, M. F. Imani, and Y. C. Eldar, "Beam focusing for near-field multiuser MIMO communications," *IEEE Transactions on Wireless Communications*, vol. 21, no. 9, pp. 7476–7490, Sep. 2022.

[18] H. Zhang, N. Shlezinger, F. Guidi, D. Dardari, and Y. C. Eldar, "6G wireless communications: From far-field beam steering to near-field beam focusing," *IEEE Communications Magazine*, vol. 61, no. 4, pp. 72–77, April 2023.

[19] A. Alkhateeb, O. El Ayach, G. Leus, and R. W. Heath, "Channel estimation and hybrid precoding for millimeter wave cellular systems," *IEEE Journal of Selected Topics in Signal Processing*, vol. 8, no. 5, pp. 831–846, 2014.

[20] J. Zhu, Z. Wan, L. Dai, M. Debbah, and H. V. Poor, "Electromagnetic Information Theory: Fundamentals, Modeling, Applications, and Open Problems," *arXiv e-prints*, p. arXiv:2212.02882, Dec. 2022.

[21] M. D. Renzo and M. D. Migliore, "Electromagnetic signal and information theory," *IEEE BITS the Information Theory Magazine*, pp. 1–13, 2024.

[22] E. Björnson, C.-B. Chae, J. Heath, Robert W., T. L. Marzetta, A. Mezghani, L. Sanguinetti, F. Rusek, M. R. Castellanos, D. Jun, and Ö. Tugfe Demir, "Towards 6G MIMO: Massive Spatial Multiplexing, Dense Arrays, and Interplay Between Electromagnetics and Processing," *arXiv e-prints*, p. arXiv:2401.02844, Jan. 2024.

[23] D. Dardari, "Reconfigurable electromagnetic environments: A general framework," *IEEE Journal on Selected Areas in Communications*, vol. 42, no. 6, pp. 1479–1493, June 2024.

[24] A. Silva, F. Monticone, G. Castaldi, V. Galdi, A. Alù, and N. Engheta, "Performing mathematical operations with metamaterials," *Science*, vol. 343, no. 6167, pp. 160–163, 2014. [Online]. Available: https://science.sciencemag.org/content/343/6167/160

[25] J. An, C. Xu, D. W. K. Ng, G. C. Alexandropoulos, C. Huang, C. Yuen, and L. Hanzo, "Stacked intelligent metasurfaces for efficient holographic MIMO communications in 6G," *IEEE Journal on Selected Areas in Communications*, vol. 41, no. 8, pp. 2380–2396, 2023.

[26] R. Harrington, "Reactively controlled directive arrays," *IEEE Trans. Antennas Propag.*, vol. 26, no. 3, pp. 390–395, May 1978.

[27] J. C. Bucheli Garcia, M. Kamoun, and A. Sibille, "Low-complexity adaptive spatial processing of ESPAR antenna systems," *IEEE Trans. Wireless Commun.*", vol. 19, no. 6, pp. 3700–3711, Feb. 2020.

[28] M. T. Ivrlac and J. A. Nossek, "Toward a circuit theory of communication," *IEEE Transactions on Circuits and Systems I: Regular Papers*, vol. 57, no. 7, pp. 1663–1683, 2010.

[29] C. A. Balanis, *Antenna Theory: Analysis and Design*. New Jersey, USA: Wiley, 2016.

[30] D. Tse and P. Viswanath, *Fundamentals of Wireless Communication*. New York, NY: Cambridge University Press, 2005.

[31] R. Fletcher, *Practical Methods of Optimization - Vol. I*. John Wiley and Sons, 1980.